

Article

Comparison of the Activity of 3D Binary or Ternary Cobalt Coatings for Hydrogen and Oxygen Evolution Reactions

Zita Sukackienė, Aldona Balčiūnaitė ^{*}, Virginija Kepenienė , Jūratė Vaičiūnienė, Giedrius Stalnionis, Vidas Pakštas, Loreta Tamašauskaitė-Tamašiūnaitė  and Eugenijus Norkus ^{*} 

Center for Physical Sciences and Technology (FTMC), Saulėtekio Ave. 3, LT-10257 Vilnius, Lithuania

* Correspondence: aldonabalcunaite@ftmc.lt (A.B.); eugenijus.norkus@ftmc.lt (E.N.)

Abstract: In this study, cobalt-nickel (Co-Ni), cobalt-iron (Co-Fe), cobalt-iron-manganese (Co-Fe-Mn), cobalt-iron-molybdenum (Co-Fe-Mo), and cobalt-zinc (Co-Zn) coatings were studied as catalysts towards the evolution of hydrogen (HER) and oxygen (OER). The binary and ternary Co coatings were deposited on a copper surface using the electroless metal plating technique and morpholine borane (MB) as a reducing agent. The as-deposited Co-Ni, Co-Fe, Co-Fe-Mn, Co-Fe-Mo, and Co-Zn coatings produce compact and crack-free layers with typical globular morphology. It was found that the Co-Fe-Mo coating gives the lowest overpotential of 128.0 mV for the HER and the lowest overpotential of 455 mV for the OER to achieve a current density of 10 mA cm^{-2} . The HER and OER current density values increase 1.4–2.0 times with an increase in temperature from 25 °C to 55 °C using the prepared 3D binary or ternary cobalt coatings for HER and OER. The highest mass electrocatalytic activity of $1.55 \text{ mA } \mu\text{g}^{-1}$ for HER and $2.72 \text{ mA } \mu\text{g}^{-1}$ for OER was achieved on the Co-Fe coating with a metal loading of $28.11 \mu\text{g cm}^{-2}$ at 25 °C.



Citation: Sukackienė, Z.; Balčiūnaitė, A.; Kepenienė, V.; Vaičiūnienė, J.; Stalnionis, G.; Pakštas, V.; Tamašauskaitė-Tamašiūnaitė, L.; Norkus, E. Comparison of the Activity of 3D Binary or Ternary Cobalt Coatings for Hydrogen and Oxygen Evolution Reactions. *Batteries* **2022**, *8*, 129. <https://doi.org/10.3390/batteries8090129>

Received: 18 July 2022

Accepted: 15 September 2022

Published: 19 September 2022

Publisher's Note: MDPI stays neutral with regard to jurisdictional claims in published maps and institutional affiliations.



Copyright: © 2022 by the authors. Licensee MDPI, Basel, Switzerland. This article is an open access article distributed under the terms and conditions of the Creative Commons Attribution (CC BY) license (<https://creativecommons.org/licenses/by/4.0/>).

Keywords: cobalt; nickel; iron; manganese; molybdenum; hydrogen evolution; oxygen evolution

1. Introduction

Population growth leads to the depletion of natural resources, which is causing an energy crisis. This problem has attracted a lot of attention for producing new and promising alternatives. Electrochemical water splitting is one of the alternative methods that can be used to solve energy problems due to its safety, cleanliness, and simplicity of the process [1,2]. Produced hydrogen (H_2) from electrochemical water splitting is like green energy; it does not involve carbon and can keep a greater energy capacity. As such, it can be seen as the up-and-coming nominee for a potential energy resource [3–8]. Hydrogen obtained using electrochemical water splitting is especially clean compared to hydrogen produced by the steam reforming process, and it is one of the most desirable alternatives to fossil fuels [9].

For more than half a century, many researchers have been looking for novel effective materials to produce H_2 from water-splitting electrolysis. Noble metals, such as Pt, Au, Ru, and Pd, have been shown to have good electrocatalytic activity in water-splitting reactions. The noble metals have available empty d orbitals and enhance the electric properties, such as high electric current and electrons mobility, leading to increasing H_2 evolution. However, noble metal catalysts are rare and expensive. For this reason, researchers tend to focus on cheaper alternatives to replace noble metal catalysts. Up to now, many water-splitting catalysts have been developed, such as transition metals [10–27], metal-oxides [13,16,17], metal-nitrides [19,20,23,24], metal-sulfides [10–12,18], metal-hydroxides [28–30], and alloys [31–36]. Many catalysts have been investigated, and researchers are still looking for catalyst fabrication methods to increase the catalyst activity for HER and OER. For example, researchers currently are designing special coatings to expose more active sites by using a conductive substrate to increase the overall conductivity, doping some atoms to optimize

the structure of the active center, and performing electrochemical activation to construct a new active phase. These works mainly aim to find more active catalysts for water-splitting electroactivity.

As mentioned above, electrochemical water-splitting can be performed by two half-reactions: HER at the cathode [37] and OER at the anode [38]. The HER is based on the formation of H₂ molecules on the cathode in acidic or alkaline solutions. In general, there are three steps for H₂ production from water splitting in an alkaline solution (Equations (1)–(3)):



The first step is called the Volmer reaction, which is for water molecules or H₂ to adsorb onto an electrode to generate MH_{ads} species (Equation (1)), and the next is to generate H₂ gas through the Heyrovsky or Tafel step (Equations (2) and (3)).

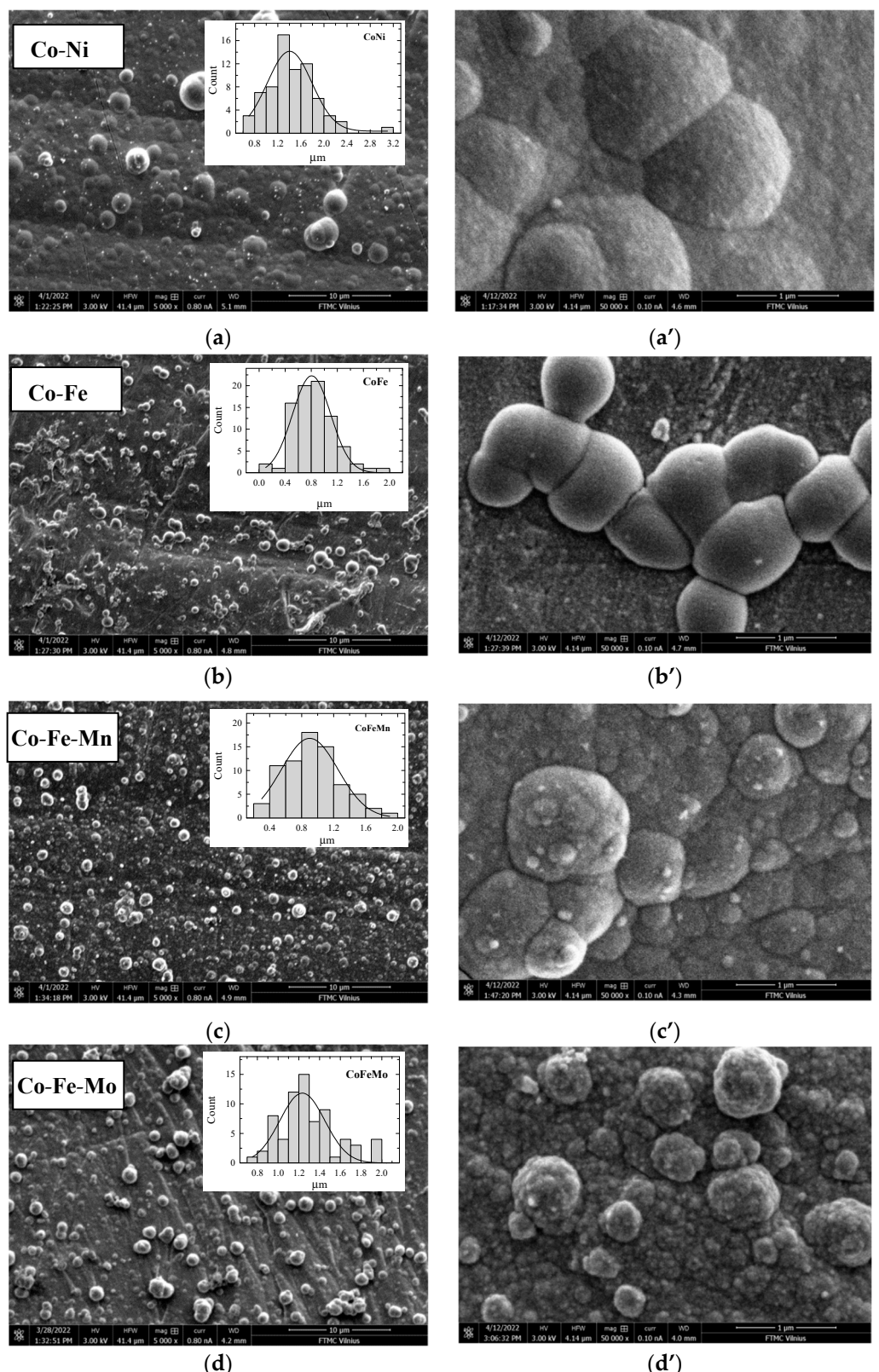
Another OER reaction occurring on the anode also needs effective and low-cost catalysts. Many researchers have focused on developing and designing catalysts with high activity, examining their long-term stability in alkaline environments. Usually, the OER process involves a complex four-electron-proton coupling reaction. Thus, OER requires a larger overpotential, which leads to OER being a key step in water splitting [39,40].

It is known that noble metals are the most efficient metal catalysts, showing excellent catalytic performance in producing high cathodic and anodic currents in acidic or alkaline electrochemical water splitting. Many researchers have focused on developing novel alternative catalysts that are cheaper and more abundant than noble metals. In this context, cobalt (Co) binary and ternary coatings with metals such as nickel (Ni), zinc (Zn), iron (Fe), manganese (Mn), tungsten (W), and molybdenum (Mo) have been investigated for their suitability as electrode material for electrochemical water splitting, i.e., HER and OER, or for both [35,38,41–47]. They are potential candidates with the extra benefit of low cost in manufacturing. It was demonstrated that binary or ternary coatings have high efficiency for water-splitting reactions as electrocatalysts [47]. Despite some significant breakthroughs, we still have many challenges to overcome in the future (descriptors of catalytic activity in alkaline solution; many substances have an amorphous structure which needs to change to crystalline, which shows better catalytic activity; deactivation of catalysts and other problems). Accordingly, we investigated the possibilities of using the binary and ternary Co coatings, i.e., Co-Ni, Co-Fe, Co-Fe-Mn, Co-Fe-Mo, and Co-Zn, deposited on the copper (Cu) substrate using a low-cost electroless metal plating method as electrocatalysts for HER and OER.

2. Results and Discussion

2.1. Characterization of Coatings

In this study, 3D binary or ternary cobalt coatings (Co-Ni, Co-Fe, Co-Zn, Co-Fe-Mn, and Co-Fe-Mo) were evaluated as electrocatalysts for HER and OER in an alkaline medium. These Co-based coatings were plated on a Cu surface using an electroless metal deposition technique and morpholine borane (MB) as a reducing agent. The coatings' surface morphology was studied by scanning electron microscopy. Figure 1 shows SEM images of the prepared Co-Ni (a), Co-Fe (b), Co-Fe-Mn (c), Co-Fe-Mo (d), and Co-Zn (e) coatings under different magnifications. The surface morphology of coatings is observed to be compact and crack-free (Figure 1a–e). The top side views of Co coatings in Figure 1a–e show a typical globular morphology consisting of larger nodulus in the average size range of ca. 1.2–1.4, 0.6–1.0, 0.8–1.2, 1.2–1.4, and 0.8–1.0 μm for Co-Ni, Co-Fe, Co-Fe-Mn, Co-Fe-Mo, and Co-Zn, respectively, while the ones consisting of smaller nodulus are in size range of ca. 0.08–0.17 μm.

**Figure 1.** *Cont.*

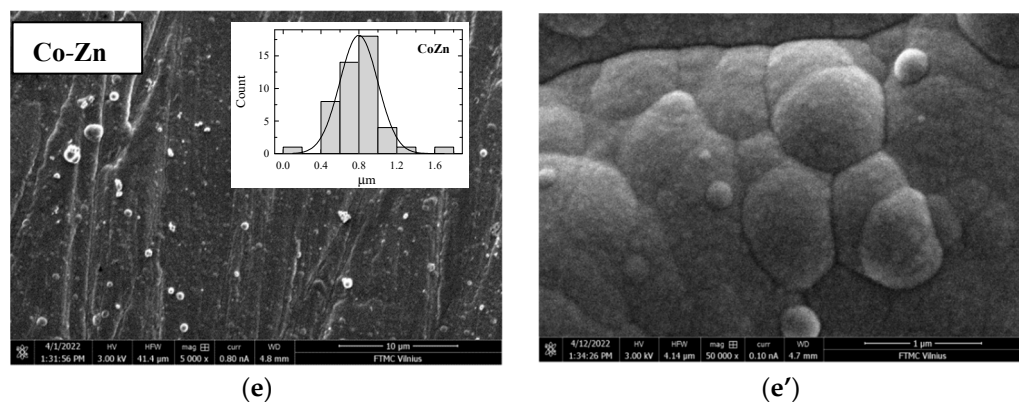


Figure 1. SEM images of as-prepared Co-Ni (**a,a'**), Co-Fe (**b,b'**), Co-Fe-Mn (**c,c'**), Co-Fe-Mo (**d,d'**), and Co-Zn (**e,e'**) coatings on Cu surfaces under different magnifications.

The data of ICP-OES analysis of deposited Co binary and ternary coatings are given in Table 1. The Co coatings were prepared with different amounts of Co. The amount of Co in the Co-Ni and Co-Fe coatings was ca. 47 and 42 at.%, respectively, whereas in the Co-Zn coating, the Co amount is significantly higher and reaches ca. 94 at.%. In the case of Co-Fe-Mn and Co-Fe-Mo coatings, the amount of Co significantly differs and is equal to ca. 28 and 86 at.%, respectively. The same observation was seen for the Fe amount in those coatings. A higher amount of ca. 71 at.% of Fe was deposited in the Co-Fe-Mn coating, and only ca. 8 at.% of Fe was incorporated in the Co-Fe-Mo coating. Additionally, the amounts of Mn and Mo of ca. 1 and 6 at.% were incorporated in the Co-Fe-Mn and Co-Fe-Mo coatings.

Table 1. ICP-OES results of the studied coatings.

Coating	At. %						Total Metal Loading ($\mu\text{g cm}^{-2}$)
	Co	Ni	Fe	Zn	Mn	Mo	
Co-Ni	47.22	52.78					526.45
Co-Fe	42.54		57.46				28.11
Co-Fe-Mn	28.07		70.83		1.09		40.58
Co-Fe-Mo	86.36		7.90			5.74	868.05
Co-Zn	93.71			6.29			351.04

The total metals loadings ($\mu\text{g cm}^{-2}$) in the prepared coatings were also quite different, varying from 28 up to 868 $\mu\text{g cm}^{-2}$. Fe ions were found to limit the rate of the electroless deposition of the Co-Fe and Co-Fe-Mn coatings. In the case of Co-Fe-Mo, the addition of Mo(VI) ions into the plating solution increases the coating deposition rate, but the concentration of Mo(VI) ions should be low (~1 mM).

The structure of Co binary and ternary coatings was evaluated using X-ray diffraction. XRD patterns of Co binary and ternary coatings were deposited on a Cu substrate with a cubic structure (ICDD #00-004-0836). Cu peaks at $2\theta = 43.3^\circ$ (111 planes), 50.43° (200), and 74.13° (220) are seen in all XRD patterns (Figure 2).

It can be stated that the crystalline peaks for Co-Fe and Co-Fe-Mn are not seen in the corresponding XRD patterns (Figure 2a). Since the electroless deposition of Co-Fe solid solution on the Cu substrate is slow, the hydrogen released during the process can lead to the formation of unstable CuH, which decomposes over time (or heating) [48]. The possible formation of CuH interfered with the formation of the Co-Fe solid solution. In the XRD pattern for the as-deposited Co-Fe coating (Figure 2c), a broad XRD peak at 40.5° related to the formation of CuH (ICDD #04-021-7878) is visible. After recording the XRD pattern for the same sample after two weeks of exposure, the mentioned peak can no longer be detected, which confirms the unstable CuH compound's possible formation during the

Co-Fe coating's electroless deposition. Moreover, the shift of the Cu (220) peak in the XRD pattern for Co-Fe coating (Figure 2a) is likely due to the roughness of the Cu substrate. Regarding the XRD patterns recorded by the grazing incidence X-ray diffraction method (grazing incidence angle = 0.5 deg.), peaks of Cu (220) may have appeared due to the non-ideal smooth/flat surface of the Cu base (the shifts are especially evident at larger 2θ angles). Co-Fe and Co-Fe-Mn coatings are very thin, so the shift of peak is not affected by the Cu surface (especially at large 2θ angles). Notably, Cu substrate peaks are not intense in the XRD patterns for Co-Zn, Co-Fe-Mo, and Co-Ni (Figure 2b), since the thicker coatings were deposited on the Cu substrate. The XRD peaks at ca. $2\theta = 44.5^\circ$ for Co-Zn, Co-Fe-Mo, and Co-Ni coatings are wide, indicating a fine crystallinity (0.5–1.5 nm) of the coatings (Figure 2b). Those peaks can be attributed to consisting of a solid solution of Co with Fe, Zn, or Ni: Co_{0.75}Fe_{0.25} (ICDD #04-003-3891), Co_{2.37}Zn_{2.63} (ICDD #01-084-3248), and Co-Ni (ICDD #01-082-3072).

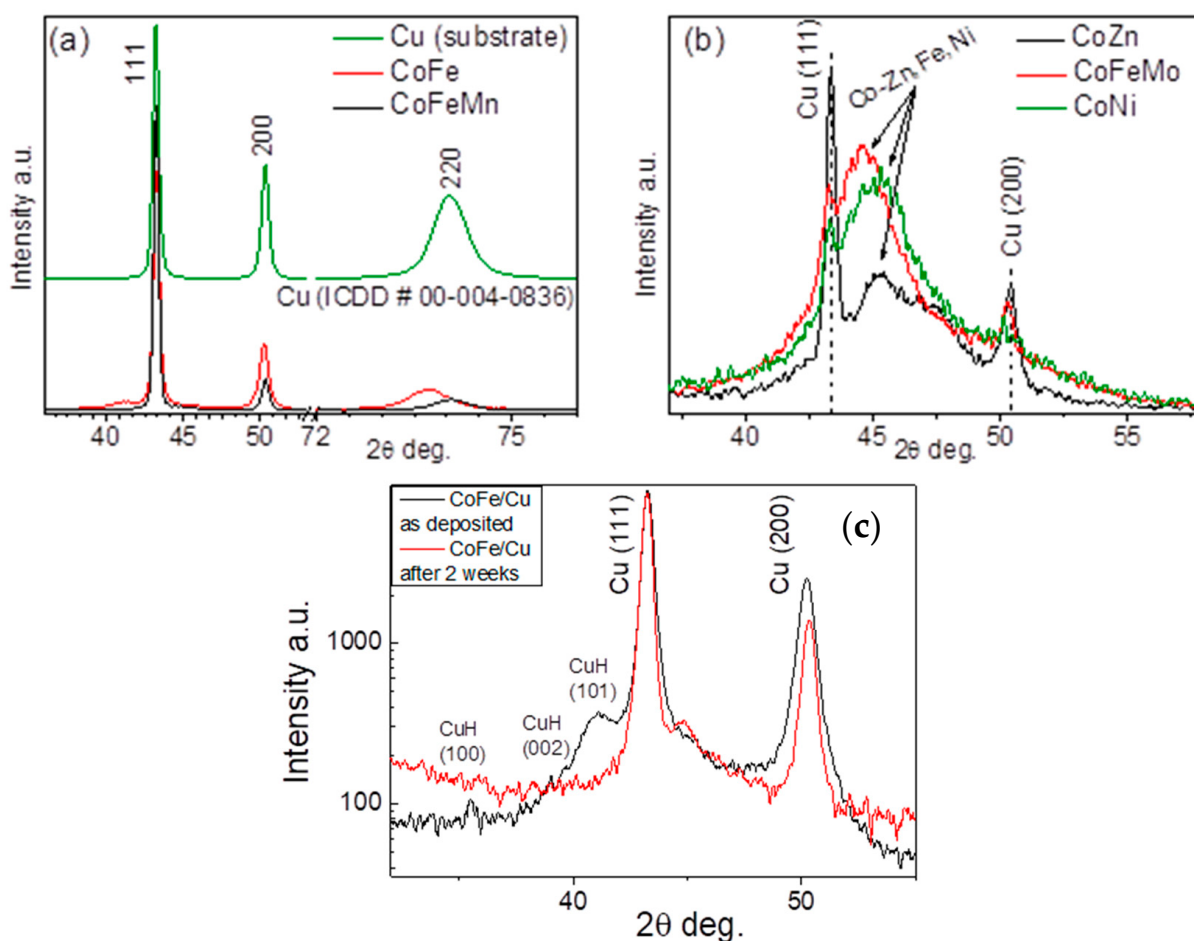


Figure 2. XRD patterns of coatings with different metals: (a) Cu (substrate), Co-Fe, and Co-Fe-Mn; (b) Co-Zn, Co-Fe-Mo, and Co-Ni. (c) represents the XRD patterns of as-deposited Co-Fe on Cu and that after 2 weeks of exposure.

2.2. Electrocatalytic Activity of Coatings for HER

The activity of the prepared catalysts for HER was investigated by recording linear sweep voltammograms (LSVs) in a 1 M KOH solution at a potential scan rate of 5 mV s^{-1} from open-circuit potential (OCP) up to -0.45 V at a temperature from 25 up to 55°C (Figure 3).

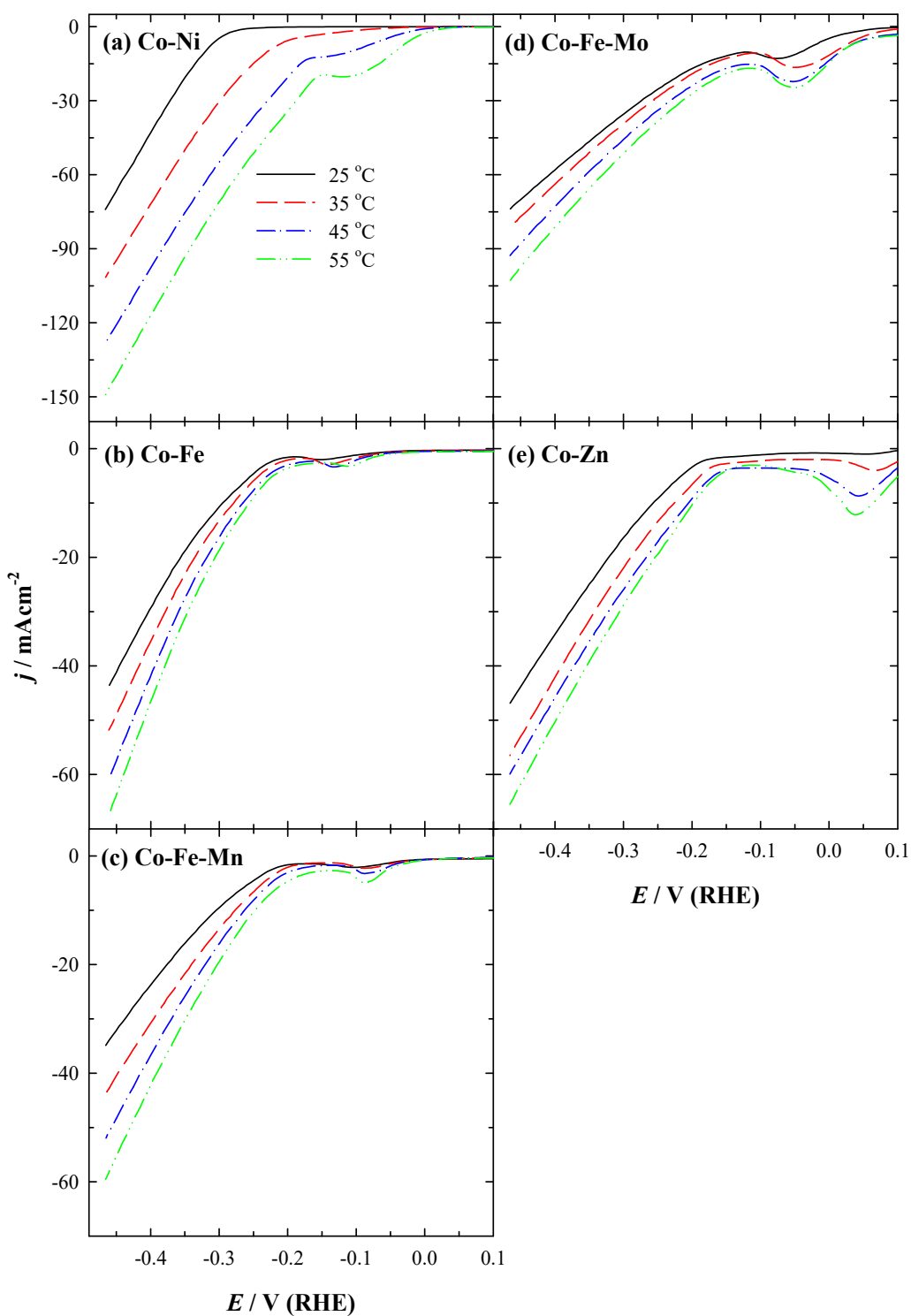


Figure 3. HER polarization curves of five studied coatings at 5 mV s^{-1} potential scan rate in 1 M KOH at different temperatures ($25\text{--}55^\circ\text{C}$): (a) Co-Ni, (b) Co-Fe, (c) Co-Fe-Mn, (d) Co-Fe-Mo, and (e) Co-Zn.

As evident from LSVs for all studied coatings, the obtained current densities at -0.45 V increase with the increase in temperature. Onset potential (E_{onset}) values for HER are shifted to more positive potential values with the increase in temperature for Co-Ni coating (Figure 3a). Co-Ni achieved the highest current density (j), followed by Co-Fe-Mo, Co-Zn, and Co-Fe coatings, and then by Co-Fe-Mn with notably lower current density during HER (Figure 3). The current density increases 1.4–2.0 times with an increase in temperature from

25 °C to 55 °C using the prepared different 3D binary or ternary cobalt coatings for HER. For instance, the current densities of -74.08 , -73.91 , -46.86 , -43.56 , and $-34.88 \text{ mA cm}^{-2}$ were reached at -0.45 V using Co-Ni, Co-Fe-Mo, Co-Zn, Co-Fe, and Co-Fe-Mn coatings, respectively, at 25 °C (Figure 4a and Table 2).

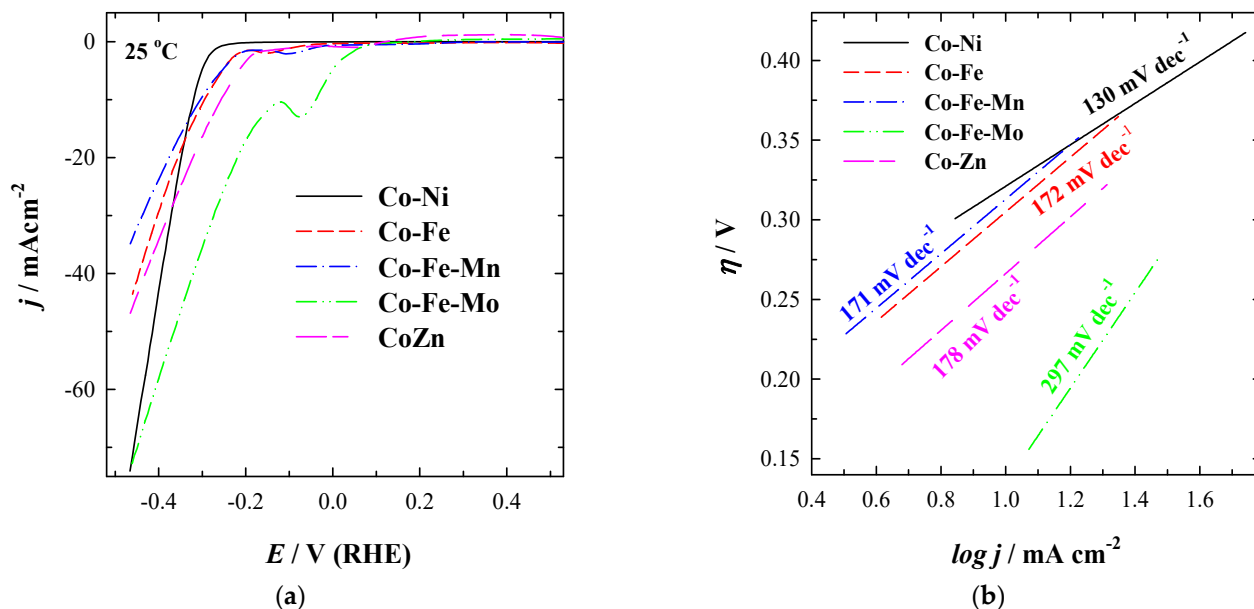


Figure 4. (a) LSVs of Co-Ni, Co-Fe, Co-Fe-Mn, Co-Fe-Mo, and Co-Zn coatings recorded in 1 M KOH at 25 °C temperature at a potential scan rate of 5 mV s^{-1} . (b) represents the corresponding Tafel plots.

Table 2. Electrochemical parameters for HER obtained on investigated cobalt coatings.

Coating	$j (\text{mA cm}^{-2})$ at Different Temperatures (°C) at -0.45 V				$j (\text{mA } \mu\text{g}^{-1})$ at $25 \text{ }^\circ\text{C}$	η_{10}^* (mV) at $25 \text{ }^\circ\text{C}$	Tafel Slope (mV Dec ⁻¹)
	25	35	45	55			
Co-Ni	-74.08	-101.52	-128.07	-149.19	0.14	-324.1	130
Co-Fe	-43.56	-51.80	-60.70	-67.35	1.55	-299.7	172
Co-Fe-Mn	-34.88	-43.87	-51.96	-59.52	0.86	-304.6	171
Co-Fe-Mo	-73.91	-81.44	-92.80	-102.86	0.09	-128.0	297
Co-Zn	-46.86	-56.49	-59.92	-65.48	0.13	-259.2	178

* Overpotential (mV) at 10 mA cm^{-2} .

The possible kinetics of HER reaction on the Co-based coatings were investigated using Tafel plots. The Tafel equation (Equation (4)) was used for the determination of the kinetic parameters for the HER:

$$\eta = a + b \log j, \quad (4)$$

where η (V), b (V dec^{-1}), j (A cm^{-2}), and a (V) represent the applied overpotential, the Tafel slope, the resulting current density, and the curve intercept, respectively. Tafel slope values were found to be 130, 172, 171, 297, and 178 mV dec⁻¹ (Figure 4b and Table 2) for the prepared 3D structured Co-Ni, Co-Fe, Co-Fe-Mn, Co-Fe-Mo, and Co-Zn 3D coatings, respectively, implying that HER might occur through the Volmer–Heyrovsky mechanism. The overpotential to reach a current density of 10 mA cm^{-2} (η_{10}) was found to be 128.0 mV for Co-Fe-Mo and increased in the order Co-Zn (259.2 mV) < Co-Fe (299.7 mV) < Co-Fe-Mn (306.4 mV) < Co-Ni (324.1 mV) (Table 2).

2.3. Electrocatalytic Activity of Coatings for OER

The activity of the prepared 3D binary or ternary Co coatings for OER was also thoroughly examined in alkaline media (1 M KOH). LSVs were recorded in a 1 M KOH

solution at a potential scan rate of 5 mV s^{-1} from open-circuit potential (OCP) up to $+2.05 \text{ V}$ vs. RHE in the temperature range of $25\text{--}55^\circ\text{C}$. OER LSVs of Co-Ni, Co-Fe, Co-Fe-Mn, Co-Fe-Mo, and Co-Zn coatings are presented in Figure 5, where it can be observed that the highest current density was achieved for the Co-Fe-Mo coating (Figure 5d).

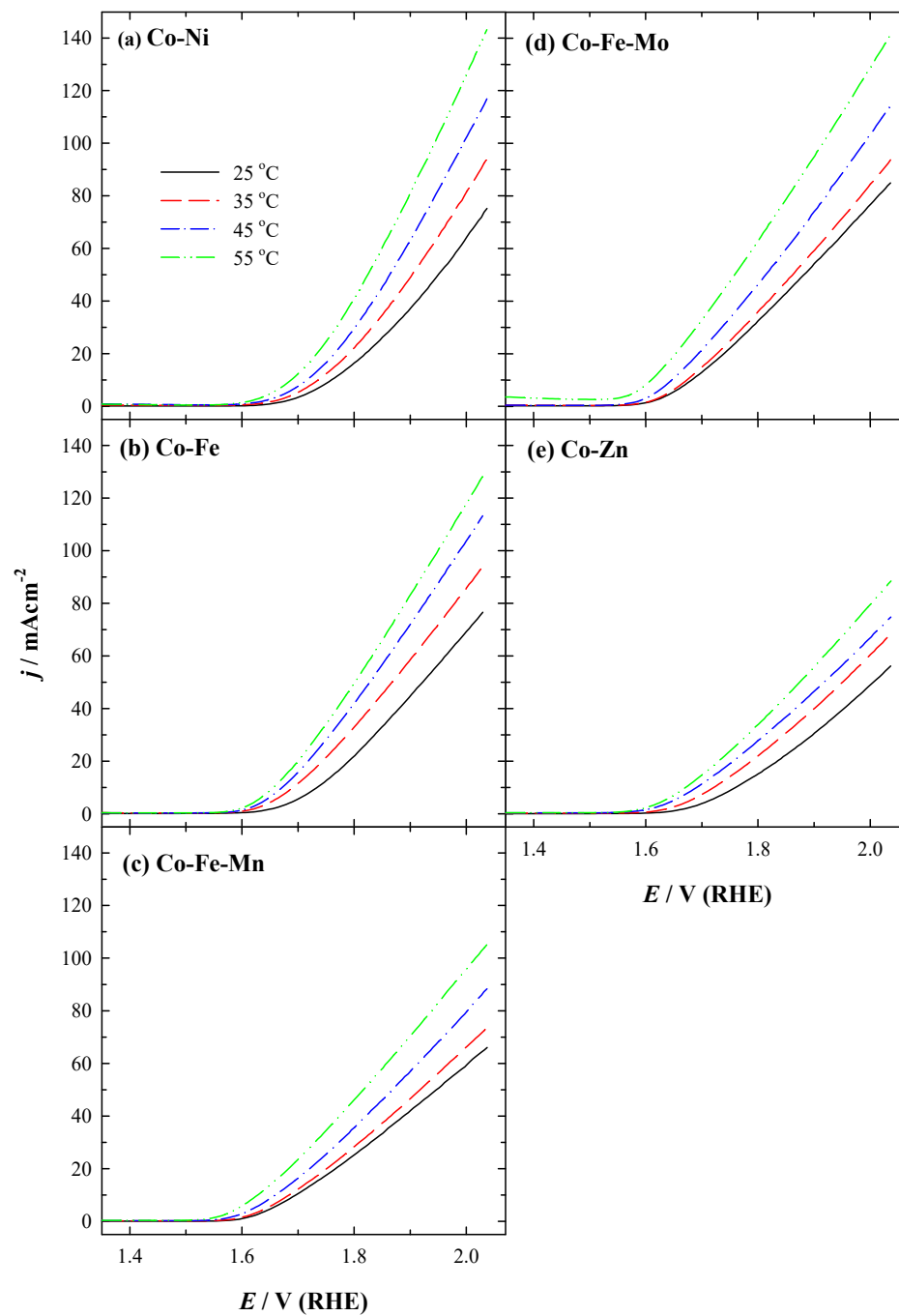


Figure 5. OER LSVs of Co-Ni, Co-Fe, Co-Fe-Mn, Co-Fe-Mo, and Co-Zn coatings recorded in 1 M KOH at different temperatures ($25\text{--}55^\circ\text{C}$) at a potential scan rate of 5 mV s^{-1} : (a) Co-Ni, (b) Co-Fe, (c) Co-Fe-Mn, (d) Co-Fe-Mo, and (e) Co-Zn.

The current density increases by 1.5–1.9 times with an increase in temperature from 25°C to 55°C using the 3D structured Co-Ni, Co-Fe, Co-Fe-Mn, Co-Fe-Mo, and Co-Zn coatings for OER. The lowest potential to reach a current density of $10 \text{ mA}\cdot\text{cm}^{-2}$ was found for Co-Fe-Mo (1.685 V), followed by a slight increase in the following order: Co-Fe-Mn (1.700 V), Co-Fe (1.737 V), Co-Zn (1.760 V), and Co-Ni (1.760 V) coatings (Table 3).

Furthermore, current density values of $50 \text{ mA} \cdot \text{cm}^{-2}$ at 25°C (Figure 6) were attained at potential values increasing in the following order: Co-Fe-Mo (1.887 V) < Co-Fe (1.923 V) < Co-Ni and Co-Fe-Mn (1.952 V) < Co-Zn (2.007 V). OER LSVs (Figure 6a) were then further used for constructing the Tafel plots and calculating the Tafel slope (Figure 6b). The lowest Tafel slope value of 54 mV dec^{-1} was found for OER at Co-Fe-Mn. Higher values of 77 , 81 , 91 and 100 mV dec^{-1} were determined for OER at Co-Fe-Mo, Co-Zn, Co-Ni, and Co-Fe, respectively (Figure 6b and Table 3).

Table 3. Electrochemical parameters for OER obtained on investigated cobalt coatings.

Coating	j (mA cm^{-2}) at Different Temperature ($^\circ\text{C}$) at $+2.05 \text{ V}$				$j (\text{mA } \mu\text{g}^{-1})$ at 25°C	η_{10}^* (V) at 25°C	Tafel Slope (mV Dec^{-1})
	25	35	45	55			
Co-Ni	75.19	94.07	116.83	143.14	0.14	1.760	81.00
Co-Fe	76.55	93.93	113.22	128.31	2.72	1.737	91.00
Co-Fe-Mn	65.99	73.59	88.35	105.22	1.63	1.700	54.00
Co-Fe-Mo	84.97	93.75	114.47	141.54	0.10	1.685	77.00
Co-Zn	56.17	68.36	74.78	88.42	0.16	1.760	77.00

* Potential (V) at 10 mA cm^{-2} .

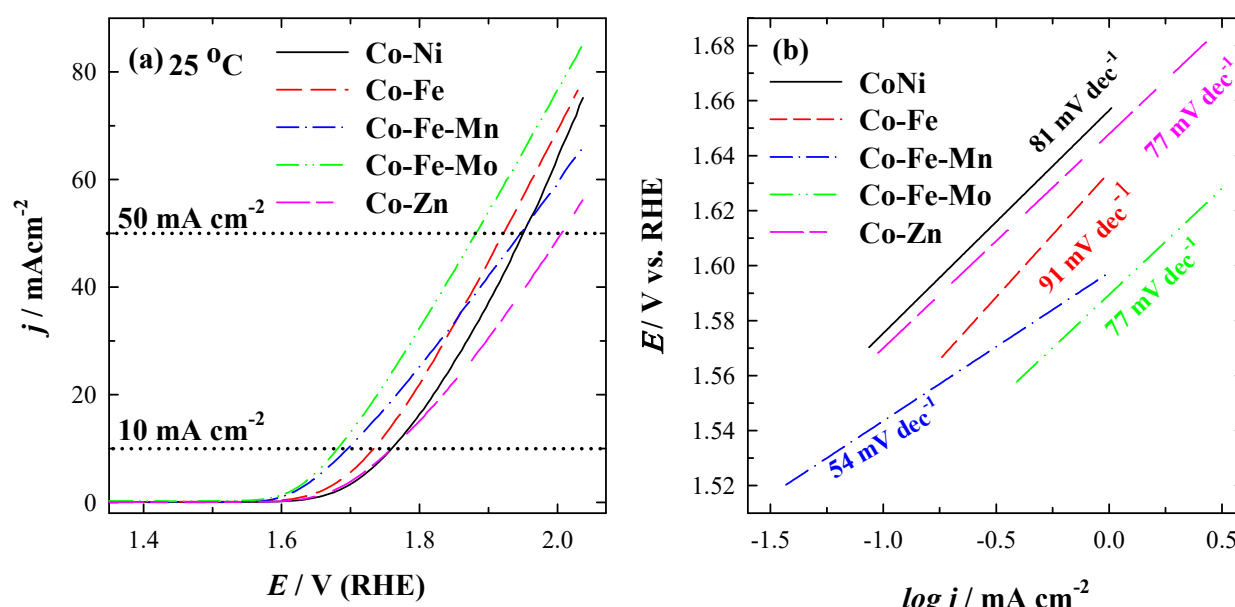


Figure 6. OER LSVs of Co-Ni, Co-Fe, Co-Fe-Mn, Co-Fe-Mo, and Co-Zn coatings recorded in 1 M KOH at 25°C temperature at a potential scan rate of 5 mV s^{-1} (a). (b) represents the corresponding Tafel plots.

The Co-Fe-Mo coating shows the best electrocatalytic performance for HER and OER among the Co-Ni, Co-Fe, Co-Fe-Mn, and Co-Zn coatings. It only needs 128 and 455 mV to achieve 10 mA cm^{-2} for HER and OER, respectively, which are significantly lower compared with those for the Co-Fe coating. The addition of Mo to the Co-Fe coating results in higher activity of the Co-Fe-Mo coating compared to pure Co-Fe. This may be related to the multiple synergistic effects among components.

In order to compare the electrocatalytic activity of these Co-based coatings, the current density values were normalized in reference to the metals loadings for each catalyst to represent the mass activity of catalysts towards the HER and OER at a temperature of 25°C (Figure 7, Tables 2 and 3). The highest mass electrocatalytic activity for HER ($1.55 \text{ mA } \mu\text{g}^{-1}$) and OER ($2.72 \text{ mA } \mu\text{g}^{-1}$) shows the Co-Fe coating with a metal loading of $28.11 \text{ } \mu\text{g cm}^{-2}$. Co-Fe-Mo, Co-Ni, and Co-Zn coatings show similar mass activity for both reactions. Co-Fe and Co-Fe-Mn coatings demonstrate ca. 19 , 27 , and 17 and 12 , 16 , and 10 times, respectively,

higher mass activity for OER than Co-Ni ($0.14 \text{ mA } \mu\text{g}^{-1}$), Co-Fe-Mo ($0.10 \text{ mA } \mu\text{g}^{-1}$), and Co-Zn ($0.16 \text{ mA } \mu\text{g}^{-1}$) coatings (Figure 7b, Table 3). In the case of HER, a higher mass activity was also obtained using Co-Fe and Co-Fe-Mn coatings. Mass activities for HER are ca. 11, 17, and 12 times higher for the Co-Fe coating as compared with those for Co-Ni, Co-Fe-Mo, and Co-Zn, respectively (Figure 7a, Table 2). Furthermore, the Co-Fe-Mn coating also exhibits ca. 6, 10, and 7 times higher mass activity for HER than those for Co-Ni, Co-Fe-Mo, and Co-Zn, respectively (Figure 7a, Table 2).

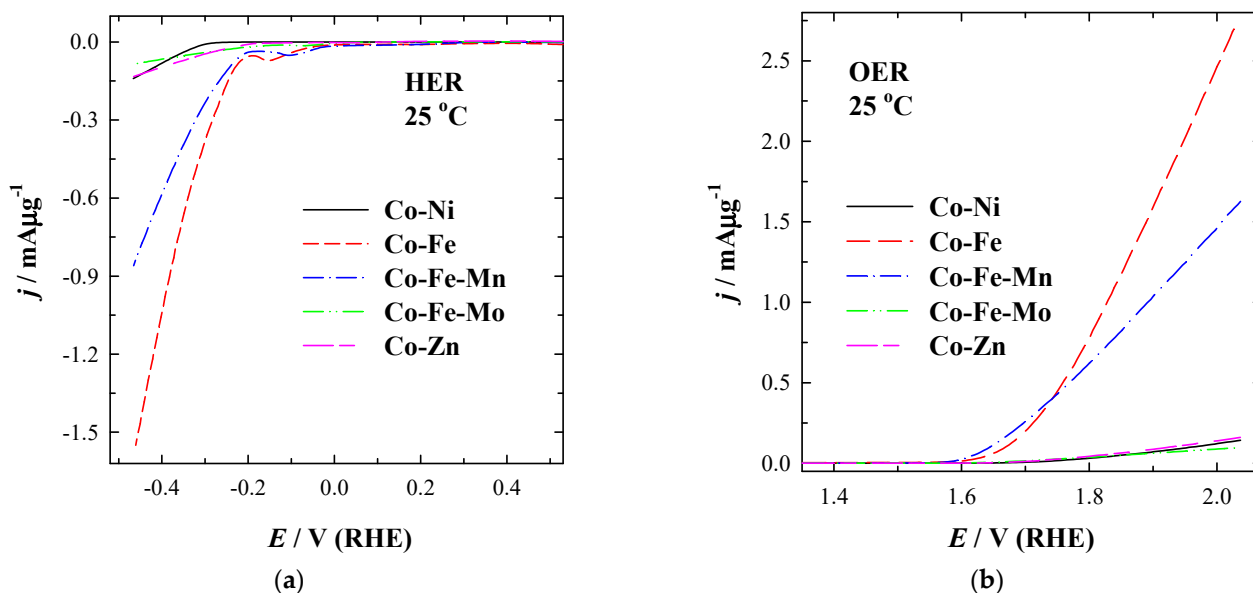


Figure 7. (a) OER and (b) HER LSVs of Co-Ni, Co-Fe, Co-Fe-Mn, Co-Fe-Mo, and Co-Zn coatings recorded in 1 M KOH at 25 °C temperature at a potential scan rate of 5 mV s⁻¹.

A comparison of HER and OER current densities generated using herein-tested Co-based coatings in an alkaline medium with some of the transition metal-based electrodes reported in the literature (Tables 4 and 5) demonstrates that the Co-based coatings exhibit comparable overpotentials and Tafel slopes for HER, but manifest similar or lower overpotentials and Tafel slopes for OER.

Table 4. Comparison of HER parameters generated on transition metal-based electrodes reported in the literature with those on the investigated Co coatings in this study.

Catalyst	η_{10}^* (mV at 25 °C)	Tafel Slope (mV Dec ⁻¹)	Electrolyte	Ref.
Co-Ni	-324.1	130	1 M KOH	This work
Co-Fe	-299.7	172	1 M KOH	This work
Co-Fe-Mn	-304.6	171	1 M KOH	This work
Co-Fe-Mo	-128.0	297	1 M KOH	This work
Co-Zn	-259.2	178	1 M KOH	This work
Co ₉ S ₈ -MoS ₂ @3DC	-177	84	1 M KOH	[39]
Co ₃ O ₄ -CuO	-288	65	1 M KOH	[40]
CoP	-163	51	1 M KOH	[41]
Ni-Co alloy	86.7	69.8	1 M KOH	[42]
Co ₃ Mo	-120	117	1 M KOH	[49]
NiFe nanosheets	-84	225	1 M KOH	[50]
β -Ni(OH) ₂	-333	230	1 M KOH	[51]

* Overpotential (mV) at 10 mA cm⁻².

Table 5. Comparison of OER parameters generated on transition metal-based electrodes reported in the literature with those on the investigated Co coatings in this study.

Catalyst	η_{10}^* (mV at 25 °C)	Tafel Slope (mV Dec ⁻¹)	Electrolyte	Ref.
Co-Ni	530	81.00	1M KOH	This work
Co-Fe	507	91.00	1M KOH	This work
Co-Fe-Mn	470	54.00	1M KOH	This work
Co-Fe-Mo	455	77.00	1M KOH	This work
Co-Zn	530	77.00	1M KOH	This work
CoFeP	350	59	1M KOH	[52]
CoFe ₂ O ₄	560	182	1M KOH	[52]
CoP	430	101	1M KOH	[52]
NiCo ₂ O ₄	470	89	0.1M KOH	[53]
Co ₃ O ₄	625	113	0.1M KOH	[53]
β -Ni(OH) ₂	498	149	1M KOH	[51]

* Overpotential (mV) at 10 mA cm⁻².

3. Materials and Methods

3.1. Preparation of Coatings

Co binary and ternary coatings were deposited on copper (Cu) (1 × 1 cm) sheets using an electroless plating bath containing metal salts, glycine (Gly), sodium acetate (CH₃COONa), and morpholine borane (MB) as a reducing agent. For Cu sheet activation prior to deposition of coatings, a PdCl₂ solution was used. The cleaned Cu sheets were dipped in a solution containing 0.5 g L⁻¹ PdCl₂ for 5 s, rinsed with deionized water, and placed into the plating bath. The composition of the plating bath and the deposition parameters of different 3D binary or ternary Co coatings are shown in Table 6. The plating time was the same for all coatings (30 min), whereas the temperature of plating baths differed for each coating.

Table 6. Plating baths and coating parameters.

Coating	Composition of Plating Baths									Plating Conditions		
	Co ²⁺ (M)	Ni ²⁺ (M)	Fe ²⁺ (M)	Mn ²⁺ (M)	Zn ²⁺ (M)	Mo ⁶⁺ (M)	MB (M)	Gly (M)	CH ₃ COO (M)	pH	t (min)	T (°C)
Co-Ni	0.06	0.15	-	-	-	-	0.05	0.2	0.04	7	30	30
Co-Fe	0.01	-	0.15	-	-	-	0.06	0.3	-	5	30	60
Co-Fe-Mn	0.07	-	0.15	0.05	-	-	0.06	0.2	-	7	30	50
Co-Fe-Mo	0.01	-	0.15	-	-	0.001	0.06	0.3	0.02	5	30	60
Co-Zn	0.07	-	-	-	0.02	-	0.06	0.2	-	7	30	45

3.2. Physical Characterization

The Co coatings surface morphology was characterized with SEM/FIB Workstation Helios Nanolab 650 (FEI, Hillsboro, OR, USA). XRD patterns of coatings were measured using an X-ray diffractometer SmartLab (Rigaku) using a graphite monochromator. The measurements were performed using in grazing incidence (GID) step scan mode (the incidence angle of the primary beam was 0.5°).

The Co coatings composition was analyzed with the spectrometer Optima 7000DV (Perkin Elmer, Waltham, MA, USA).

3.3. Electrochemical Measurements

The activity of Co binary and ternary coatings towards HER and OER was evaluated by linear sweep voltammetry (LSV) using a potentiostat/galvanostat PGSTAT100 (Metrohm Autolab B.V., Utrecht, The Netherlands) and a standard three-electrode electrochemical cell. The prepared 3D binary or ternary Co coatings with a geometric area of 2 cm² were used as the working electrodes. Counter and reference electrodes were a Pt sheet and

Ag/AgCl/KCl (3 M KCl) electrode, respectively. LSVs were recorded using an N₂-saturated 1 M KOH solution at the temperature range from 25 °C to 55 °C at a potential scan rate of 5 mV s⁻¹. The current densities were normalized by the geometric area of the electrodes.

4. Conclusions

The electroless metal deposition has been used for the plating of the 3D binary or ternary cobalt coatings on a copper surface. The surface morphology of Co-Ni, Co-Fe, Co-Fe-Mn, Co-Fe-Mo, and Co-Zn coatings is compact and crack-free, with typical globular morphology. The electroactivity of the prepared coatings towards the hydrogen and oxygen evolution has been investigated in alkaline media. The lowest overpotential for the HER to reach a current density of 10 mA cm⁻² has been found to be 128.0 mV for the Co-Fe-Mo coating. Furthermore, the lowest overpotential of 455 mV for the OER to reach 10 mA cm⁻² also gives the Co-Fe-Mo coating. On the other hand, adding Mo to the Co-Fe coating results in higher activity of the Co-Fe-Mo coating compared to pure Co-Fe.

The current density increases 1.4–2.0 times with an increase in temperature from 25 °C to 55 °C using the prepared 3D binary or ternary cobalt coatings for HER and OER. The highest mass electrocatalytic activity of 1.55 mA µg⁻¹ for HER and 2.72 mA µg⁻¹ for OER has been achieved on the Co-Fe coating with a metal loading of 28.11 µg cm⁻² at 25 °C.

Author Contributions: Conceptualization, Z.S., A.B., and E.N.; methodology, J.V., G.S., and V.P.; formal analysis, J.V., G.S., and V.P.; investigation, Z.S., A.B., and V.K.; writing—original draft preparation, A.B. and Z.S.; writing—review and editing, L.T.-T. and E.N.; visualization, V.K. and L.T.-T. All authors have read and agreed to the published version of the manuscript.

Funding: This research was funded by the European Social Fund under Measure No. 09.3.3-LMT-K-712-19-0138 ‘Development of Competences of Scientists, other Researchers and Students through Practical Research Activities’.

Institutional Review Board Statement: Not applicable.

Informed Consent Statement: Not applicable.

Data Availability Statement: Not applicable.

Conflicts of Interest: The authors declare no conflict of interest.

References

- Shi, H.; Zhou, Y.T.; Yao, R.Q.; Wan, W.B.; Ge, X.; Zhang, W.; Wen, Z.; Lang, X.Y.; Zheng, W.T.; Jiang, Q. Spontaneously separated intermetallic Co₃Mo from nanoporous copper as versatile electrocatalysts for highly efficient water splitting. *Nat. Commun.* **2020**, *11*, 1–10. [[CrossRef](#)] [[PubMed](#)]
- Wang, H.; Lee, H.W.; Deng, Y.; Lu, Z.; Hsu, P.C.; Liu, Y.; Lin, D.; Cui, Y. Bifunctional non-noble metal oxide nanoparticle electrocatalysts through lithium-induced conversion for overall water splitting. *Nat. Commun.* **2015**, *6*, 1–8. [[CrossRef](#)] [[PubMed](#)]
- Jiao, Y.; Zheng, Y.; Jaroniec, M.; Qiao, S.Z. Design of electrocatalysts for oxygen-and hydrogen-involving energy conversion reactions. *Chem. Soc. Rev.* **2015**, *44*, 2060–2086. [[CrossRef](#)] [[PubMed](#)]
- Ali, M.; Pervaiz, E.; Noor, T.; Rabi, O.; Zahra, R.; Yang, M. Recent advancements in MOF-based catalysts for applications in electrochemical and photoelectrochemical water splitting: A review. *Int. J. Energy Res.* **2021**, *45*, 1190–1226. [[CrossRef](#)]
- Lubitz, W.; Tumas, W. Hydrogen: An Overview. *Chem. Rev.* **2007**, *107*, 3900–3903. [[CrossRef](#)]
- Zhang, Z.; Cong, L.; Yu, Z.; Qu, L.; Huang, W. Facile synthesis of Fe–Ni bimetallic N-doped carbon framework for efficient electrochemical hydrogen evolution reaction. *Mater. Today Energy* **2020**, *16*, 100387–100394. [[CrossRef](#)]
- Yang, L.; Liu, R.; Jiao, L. Electronic Redistribution: Construction and Modulation of Interface Engineering on CoP for Enhancing Overall Water Splitting. *Adv. Funct. Mater.* **2020**, *30*, 1909618. [[CrossRef](#)]
- Zeng, K.; Zhang, D. Recent progress in alkaline water electrolysis for hydrogen production and applications. *Prog. Energy Combust. Sci.* **2010**, *36*, 307–326. [[CrossRef](#)]
- Rabi, O.; Pervaiz, E.; Zahra, R.; Ali, M.; Niazi, B.K. An inclusive review on the synthesis of molybdenum carbide and its hybrids as catalyst for electrochemical water splitting. *Mol. Catal.* **2020**, *494*, 111116–111135. [[CrossRef](#)]
- Shah, S.A.; Xu, L.; Sayyar, R.; Bian, T.; Liu, Z.; Yuan, A.; Shen, X.; Khan, I.; Tahir, A.A.; Ullah, H. Growth of MoS₂ nanosheets on M@N-doped carbon particles (M = Co, Fe or CoFe Alloy) as an efficient electrocatalyst toward hydrogen evolution reaction. *Chem. Eng. J.* **2022**, *428*, 132126. [[CrossRef](#)]

11. Shah, S.A.; Sayyar, R.; Xu, L.; Sun, H.; Khan, I.; Guo, J.; Shen, X.; Hussain, S.; Yuan, A.; Ullah, H. In-situ synthesis of NiS₂ nanoparticles/MoS₂ nanosheets hierarchical sphere anchored on reduced graphene oxide for enhanced electrocatalytic hydrogen evolution reaction. *J. Colloid Interface Sci.* **2022**, *624*, 150–159. [[CrossRef](#)] [[PubMed](#)]
12. Xu, L.; Shah, S.A.; Khan, H.; Sayyar, R.; Shen, X.; Khan, I.; Yuan, A.; Yaseen, W.; Ghazi, Z.A.; Naeem, A.; et al. Ni₃S₂ nanostrips@FeNi-NiFe₂O₄ nanoparticles embedded in N-doped carbon microsphere: An improved electrocatalyst for oxygen evolution reaction. *J. Colloid Interface Sci.* **2022**, *617*, 1–10. [[CrossRef](#)] [[PubMed](#)]
13. Zhang, J.; Wang, T.; Liu, P.; Liao, Z.; Liu, S.; Zhuang, X.; Chen, M.; Zschech, E.; Feng, X. Efficient Hydrogen Production on MoNi₄ Electrocatalysts with Fast Water Dissociation Kinetics. *Nat. Commun.* **2017**, *8*, 15437. [[CrossRef](#)] [[PubMed](#)]
14. Li, C.; Gao, H.; Wan, W.; Mueller, T. Mechanisms for Hydrogen Evolution on Transition Metal Phosphide Catalysts and a Comparison to P(111). *Phys. Chem. Chem. Phys.* **2019**, *21*, 24489–24498. [[CrossRef](#)]
15. Miao, R.; Dutta, B.; Sahoo, S.; He, J.; Zhong, W.; Cetegen, S.A.; Jiang, T.; Alpay, S.P.; Suib, S.L. Mesoporous Iron Sulfide for Highly Efficient Electrocatalytic Hydrogen Evolution. *J. Am. Chem. Soc.* **2017**, *139*, 13604–13607. [[CrossRef](#)]
16. Ola, O.; Ullah, H.; Chen, Y.; Thummavichai, K.; Wang, N.; Zhu, Y. DFT and experimental studies of iron oxide-based nanocomposites for efficient electrocatalysis. *J. Mater. Chem. C* **2021**, *9*, 6409–6417. [[CrossRef](#)]
17. Zhang, J.; Shang, X.; Ren, H.; Chi, J.; Fu, H.; Dong, B.; Liu, C.; Chai, Y. Modulation of Inverse Spinel Fe₃O₄ by Phosphorous Doping as an Industrially Promising Electrocatalysts for Hydrogen Evolution. *Adv. Mater.* **2019**, *31*, 1905107. [[CrossRef](#)]
18. Zhu, L.; Liu, L.; Huang, G.; Zhao, Q. Hydrogen Evolution over N-Doped CoS₂ Nanosheets Enhanced by Superaerophobicity and Electronic Modulation. *Appl. Surf. Sci.* **2020**, *504*, 144490. [[CrossRef](#)]
19. Xu, Z.; Li, W.; Yan, Y.; Wang, H.; Zhu, H.; Zhao, M.; Yan, S.; Zou, Z. In-Situ Formed Hydroxide Accelerating Water Dissociation Kinetics on Co₃N for Hydrogen Production in Alkaline Solution. *ACS Appl. Mater. Interfaces* **2018**, *10*, 22102–22109. [[CrossRef](#)]
20. Zhu, J.; Liu, X.; Wang, G. Tailoring the D-Band Centers Enables Co₄N Nanosheets to Be Highly Active for Hydrogen Evolution Catalysis. *Angew. Chem. Int. Ed. Engl.* **2018**, *57*, 5076–5080.
21. Wexler, R.B.; Martinez, J.M.P.; Rappe, A.M. Active Role of Phosphorus in the Hydrogen Evolving Activity of Nickel Phosphide (001). *Surf. ACS Catal.* **2017**, *7*, 7718–7725. [[CrossRef](#)]
22. Cao, X.; Jia, D.; Li, D.; Cui, L.; Liu, J. One-Step Co-Electrodeposition of Hierarchical Radial Ni_xP nanospheres on Ni Foam as Highly Active Flexible Electrodes for Hydrogen Evolution Reaction and Supercapacitor. *Chem. Eng. J.* **2018**, *348*, 310–318. [[CrossRef](#)]
23. Pei, Y.; Rezact, B.; Zhang, X.; Li, Z.; Shen, H.; Yang, M.; Wang, J. Interface Catalysis by Pt nanocluster@Ni₃N for Bifunctional Hydrogen Evolution and Oxygen Evolution. *Mater. Chem. Front.* **2020**, *4*, 2665–2672. [[CrossRef](#)]
24. Liu, B.; He, B.; Peng, H.Q.; Zhao, Y.; Cheng, J.; Xia, J.; Shen, J.; Ng, T.W.; Meng, X.; Lee, C.S.; et al. Unconventional Nickel Nitride Enriched with Nitrogen Vacancies as a High-Efficiency Electrocatalyst for Hydrogen Evolution. *Adv. Sci.* **2018**, *5*, 1800406. [[CrossRef](#)]
25. Ray, C.; Lee, S.C.; Jin, B.; Kundu, A.; Park, J.H.; Jun, S.C. Conceptual Design of Three-Dimensional CoN/Ni₃N-Coupled Nanograsses Integrated on N-Doped Carbonto Serve as Efficient and Robust Water Splitting Electrocatalysts. *J. Mater. Chem. A* **2018**, *6*, 4466–4476. [[CrossRef](#)]
26. Li, Z.; Feng, Y.; Liang, Y.L.; Cheng, C.Q.; Dong, C.K.; Liu, H.; Du, X.W. Stable Rhodium (IV) Oxide for Alkaline Hydrogen Evolution Reaction. *Adv. Mater.* **2019**, *32*, 1908521. [[CrossRef](#)]
27. Bae, S.Y.; Mahmood, J.; Jeon, I.Y.; Baek, J.B. Recent Advances in Ruthenium Based Electrocatalysts for the Hydrogen Evolution Reaction. *Nanoscale Horiz.* **2020**, *5*, 43–56. [[CrossRef](#)]
28. Kyeong, Y.; Woo, K.; Jun, T.; Youn, D.H.; Lee, J.S. Metal substrates activate NiFe(oxy)hydroxide catalysts for efficient oxygen evolution reaction in alkaline media. *J. Alloys Compd.* **2022**, *901*, 163689.
29. Xu, Y.; Ren, K.; Xu, R. In situ formation of amorphous Fe-based bimetallic hydroxides from metal-organic frameworks as efficient oxygen evolution catalysts. *Chin. J. Catal.* **2021**, *42*, 1370–1378. [[CrossRef](#)]
30. Loh, A.; Li, X.; Taiwo, O.O.; Tariq, F.; Brandon, N.P.; Wang, P.; Xu, K.; Wang, B. Development of Ni–Fe based ternary metal hydroxides as highly efficient oxygen evolution catalysts in AEM water electrolysis for hydrogen production. *Int. J. Hydrogen Energy* **2020**, *45*, 24232–24247. [[CrossRef](#)]
31. Zheng, Y.; Shang, P.; Pei, F.; Ma, G.; Ye, Z.; Peng, X.; Li, D. Achieving an efficient hydrogen evolution reaction with a bicontinuous nanoporous PtNiMg alloy of ultralow Noble-metal content at an ultrawide range of current densities. *Chem. Eng. J.* **2022**, *433*, 134571. [[CrossRef](#)]
32. Kamali, S.; Zhiani, M.; Tavakol, H. Synergism effect of first row transition metals in experimental and theoretical activity of NiM/rGO alloys at hydrogen evolution reaction in alkaline electrolyzer. *Renew. Energy* **2020**, *154*, 1122–1131. [[CrossRef](#)]
33. Wang, M.; Wang, Y.; Mao, S.S.; Shen, S. Transition-metal alloy electrocatalysts with active sites modulated by metal-carbide heterophases for efficient oxygen evolution. *Nano Energy* **2021**, *88*, 106216. [[CrossRef](#)]
34. Akbayrak, M.; Önal, A.M. Metal oxides supported cobalt nanoparticles: Active electrocatalysts for oxygen evolution reaction. *Electrochim. Acta* **2021**, *393*, 139053. [[CrossRef](#)]
35. Wang, R.; Li, F.; Ji, J.; Wang, F. CoMoO₄ enhanced anodized cobalt oxide nanotube as an efficient electrocatalyst for hydrogen evolution reaction. *Appl. Surf. Sci.* **2022**, *579*, 152128. [[CrossRef](#)]
36. Zhao, H.; Yuan, Z.-Y. Surface/interface engineering of high-efficiency noble metal-free electrocatalysts for energy-related electrochemical reactions. *J. Energy Chem.* **2021**, *54*, 89–104. [[CrossRef](#)]

37. Xu, H.; Zhao, Y.; He, G.; Chen, H. Race on engineering noble metal single-atom electrocatalysts for water splitting. *Int. J. Hydrogen Energy* **2022**, *47*, 14257–14279. [[CrossRef](#)]
38. Gong, Y.; Yao, J.; Wang, P.; Li, Z.; Zhou, H.; Xu, C. Perspective of hydrogen energy and recent progress in electrocatalytic water splitting. *Chin. J. Chem. Eng.* **2022**, *43*, 282–296. [[CrossRef](#)]
39. Diao, L.; Zhang, B.; Sun, Q.; Wang, N.; Zhao, N.; Shi, C.; Liu, E.; He, C. An in-plane $\text{Co}_9\text{S}_8@\text{MoS}_2$ heterostructure for the hydrogen evolution reaction in alkaline media. *Nanoscale* **2019**, *11*, 21479–21486. [[CrossRef](#)]
40. Tahira, A.; Ibrupoto, Z.H.; Willander, M.; Nur, O. Advanced Co_3O_4 -CuO nano-composite based electrocatalysts for efficient hydrogen evolution reaction in alkaline media. *Int. J. Hydrogen Energy* **2019**, *44*, 26148–26157. [[CrossRef](#)]
41. Du, Y.; Wang, Z.; Li, H.; Han, Y.; Liu, Y.; Yang, Y.; Liu, Y.; Wan, L. Controllable synthesized CoP-MP (M = Fe, Mn) as efficient and stable electrocatalyst for hydrogen evolution reaction at all pH values. *Int. J. Hydrogen Energy* **2019**, *44*, 19978–19985. [[CrossRef](#)]
42. Zhang, X.; Li, Y.; Guo, Y.; Hu, A.; Li, M.; Hang, T.; Ling, H. 3D hierarchical nanostructured Ni-Co alloy electrodes on porous nickel for hydrogen evolution reaction. *Int. J. Hydrogen Energy* **2019**, *44*, 29946–29955. [[CrossRef](#)]
43. Safizadeh, F.; Ghali, E.; Houlachi, G. Electrocatalysis developments for hydrogen evolution reaction in alkaline solutions—A review. *Int. J. Hydrogen Energy* **2015**, *40*, 256–274. [[CrossRef](#)]
44. Lu, X.; Zhao, C. Electrodeposition of hierarchically structured three-dimensional nickel-iron electrodes for efficient oxygen evolution at high current densities. *Nat. Commun.* **2015**, *6*, 6616. [[CrossRef](#)]
45. Allam, M.; Bencha, M.; Dakhouche, A. Electrodeposition and characterization of NiMoW alloy as electrode material for hydrogen evolution in alkaline water electrolysis. *Int. J. Hydrogen Energy* **2018**, *43*, 3394–3405. [[CrossRef](#)]
46. Neethu, R.M.; Hegde, A.C. Development of Ni-W alloy coatings and their electrocatalytic activity for water splitting reaction. *Phys. B* **2020**, *597*, 412359. [[CrossRef](#)]
47. Wang, S.; Lu, A.; Zhong, C.-J. Hydrogen production from water electrolysis: Role of catalysts. *Nano Converg.* **2021**, *8*, 1–23. [[CrossRef](#)]
48. Vaškelis, A.; Juškėnas, R.; Jačiauskienė, J. Copper hydride formation in the electroless copper plating process: In situ X-ray diffraction evidence and electrochemical study. *Electrochim. Acta* **1998**, *43*, 1061–1066. [[CrossRef](#)]
49. Sun, Y.; Ganin, A.Y. The synergistic effects of alloying on the performance and stability of Co_3Mo and Co_7Mo_6 for the electrocatalytic hydrogen evolution reaction. *Hydrogen* **2020**, *1*, 11–21. [[CrossRef](#)]
50. Asraf, M.A.; Kiu, Z.; Pham, B.T.; Zhang, D. Electrodeposition of superhydrophilic and binder-free Mo doped Ni-Fe nanosheets as cost-efficient bifunctional electrocatalyst for overall water splitting. *J. Electroanal. Chem.* **2020**, *873*, 114351. [[CrossRef](#)]
51. Balčiūnaitė, A.; Upadhyay, K.K.; Radinovic, K.; Santos, D.M.F.; Montemor, M.F.; Šljukic, B. Steps towards highly-efficient water splitting and oxygen reduction using nanostructured $\beta\text{-Ni(OH)}_2$. *RSC Adv. R. Soc. Chem.* **2022**, *12*, 10020–10028. [[CrossRef](#)] [[PubMed](#)]
52. Du, Y.; Qu, H.; Liu, Y.; Han, Y.; Wang, L.; Dong, B. Bimetallic CoFeP hollow microspheres as highly efficient bifunctional electrocatalysts for overall water splitting in alkaline media. *Appl. Surf. Sci.* **2019**, *465*, 816–823. [[CrossRef](#)]
53. Bejar, J.; Alvarez-Contreras, L.; Ledesma-Garcia, J.; Arjona, N.; Arriaga, L.G. Electrocatalytic evaluation of Co_3O_4 and NiCo_2O_4 rosettes-like hierarchical spinel as bifunctional materials for oxygen evolution (OER) and reduction (ORR) reactions in alkaline media. *J. Electroanal. Chem.* **2019**, *847*, 113190. [[CrossRef](#)]